

A Liquid-Nitrogen-Cooled $^{40}\text{Ca}^+$ Ion Optical Clock with a Systematic Uncertainty of 4.6×10^{-19}

Baolin Zhang,^{1,*} Zixiao Ma,^{1,2,*} Yao Huang,^{1,†} Huili Han,¹ Rumeng Hu,^{1,2} Yuzhuo Wang,^{1,2} Huaqing Zhang,¹ Liyan Tang,¹ Tingyun Shi,¹ Hua Guan,^{1,3,4,‡} and Kelin Gao^{1,3,§}

¹*State Key Laboratory of Magnetic Resonance and Atomic and Molecular Physics, Innovation Academy for Precision Measurement Science and Technology, Chinese Academy of Sciences, Wuhan 430071, China*

²*University of Chinese Academy of Sciences, Beijing 100049, China*

³*Hefei National Laboratory, University of Science and Technology of China, Hefei, 230088, China*

⁴*Wuhan Institute of Quantum Technology, Wuhan 430206, China*

(Dated: July 4, 2025)

We report a single-ion optical clock based on the $4\text{S}_{1/2} \rightarrow 3\text{D}_{5/2}$ transition of the $^{40}\text{Ca}^+$ ion, operated in a liquid nitrogen cryogenic environment, achieving a total systematic uncertainty of 4.6×10^{-19} . We employ a refined temperature evaluation scheme to reduce the frequency uncertainty due to blackbody radiation (BBR), and the 3D sideband cooling has been implemented to minimize the second-order Doppler shift. We have precisely determined the average Zeeman coefficient of the $^{40}\text{Ca}^+$ clock transition to be $14.345(40) \text{ Hz/mT}^2$, thereby significantly reducing the quadratic Zeeman shift uncertainty. Moreover, the cryogenic environment enables the lowest reported heating rate due to ambient electric field noise in trapped-ion optical clocks.

Introduction—Optical frequency is currently the physical quantity with the highest measurement precision. Over the past two decades, with the advancement of atomic and optical physics theories as well as laser technology [1–11], optical clocks have undergone substantial improvements. At present, many optical clocks have achieved uncertainties at the order of 10^{-18} or even 10^{-19} [12–20], enabling optical clocks to play an irreplaceable role in the field of precision measurement, such as investigating whether the fine-structure constant α varies over time [21], testing Lorentz invariance [22, 23], and detecting gravitational waves and dark matter [24, 25]. Meanwhile, the ultra-high precision of optical clocks is driving the redefinition of the SI second [26] and has further promoted their applications in navigation and geodesy [27–29].

The Ca^+ ion features a simple energy level structure and requires relatively fewer numbers of lasers with weaker power [30, 31]. Moreover, it has a magic trapping RF (radio frequency) that one can cancel the micromotion-induced Doppler and Stark shifts, making it one of the ideal optical clock candidates approaching very low total systematic uncertainty [2, 32]. The main contributor to the systematic uncertainty of the $^{40}\text{Ca}^+$ ion optical clock is the BBR shift. To address this, we previously utilized a liquid-nitrogen cooling scheme to reduce the BBR shift uncertainty to 2.7×10^{-18} [16]. However, due to the accuracy of the temperature evaluation, the BBR shift remains the largest contributor to the total systematic uncertainty [16, 33]. Additionally, the second-order Doppler shift arising from secular motion is also one of the main factors restricting the further reduction of the total systematic uncertainty of the $^{40}\text{Ca}^+$ ion optical clock to the 10^{-19} level [16].

In this Letter, we report on the research progress of

the second-generation liquid-nitrogen cryogenic ion optical clock Ca^{+2} (LNCIOC Ca^{+2}), which has achieved a total systematic uncertainty of 4.6×10^{-19} . This is mainly attributed to our improvements in the design and installation scheme of the BBR cavity and ion trap, the incorporation of 3D sideband cooling, and the precise measurement of the quadratic Zeeman coefficient for the $^{40}\text{Ca}^+$ ion’s clock transition.

The setup is illustrated in Fig. S1(a), and details of the trap device can be found in references [9, 16]. The trap RF frequency is set at 24.801 MHz, which is close to the magic trapping frequency [32, 34]. A DC voltage of 160 V is applied to both endcap electrodes. To separate the two secular motion frequencies in radial directions thus enabling effective sideband cooling for all 3 motional modes, we apply DC voltages of $\pm 8 \text{ V}$ to the two RF coupled electrodes. Additionally, RF amplitude stabilization is introduced to stabilize the radial secular motion frequencies, with a long-term drift of less than 2 kHz [35]. The excess micromotion (EMM) of the ion is evaluated through the sideband spectra observed by three mutually orthogonal clock laser beams (beam 1, 2, and 3 in Fig. S1(b)) and is suppressed by optimizing the voltages applied to the compensation electrodes. The vacuum system of the liquid-nitrogen cryogenic optical clock is surrounded by four layers of magnetic shielding to reduce the magnetic field noise [36]. All lasers used in LNCIOC Ca^{+2} are shown in Fig. S1(b). The quantization axis is along the y axis direction with a magnetic field of approximately $37.2 \mu\text{T}$.

The pulse sequence begins with a 1.5-ms-long Doppler cooling. Then the $^{40}\text{Ca}^+$ ion is optically pumped into one of the two sub-levels of the $\text{S}_{1/2}$ state using the 397 nm σ^+/σ^- lasers, achieving a state-preparation efficiency exceeding 99% within a 5- μs pulse length. Subsequently,

the $^{40}\text{Ca}^+$ ion is further cooled to near the 3D motional ground state through resolved sideband cooling (10 ms). To avoid the AC Stark shift, all lasers except the clock laser are blocked using mechanical shutters during the clock interrogation. The clock transition is probed with a hyper Ramsey scheme, employing a π -pulse duration of 4 ms and a free evolution time of 80 ms [1, 37]. Finally, a 2-ms-long state detection pulse is performed to determine the ion's final state.

During the clock operation, we alternately lock the clock laser onto three pairs of Zeeman transitions: $|S_{1/2}, m = \mp 1/2\rangle \rightarrow |D_{5/2}, m = \mp 3/2\rangle$, $|S_{1/2}, m = \pm 1/2\rangle \rightarrow |D_{5/2}, m = \mp 1/2\rangle$, and $|S_{1/2}, m = \mp 1/2\rangle \rightarrow |D_{5/2}, m = \mp 5/2\rangle$, to cancel out the first-order Zeeman shift, the electric quadrupole shift, and the tensor Stark shift [32, 34].

Blackbody radiation shift—The BBR shift can be expressed as [38, 39]:

$$\Delta\nu_{\text{BBR}} = -\frac{1}{2} (831.9 \text{ V m}^{-1})^2 \left(\frac{T(\text{K})}{300} \right)^4 \Delta\alpha_0 (1 + \eta), \quad (1)$$

where T is the ambient temperature, $\Delta\alpha_0$ is the differential static polarizability for the $^{40}\text{Ca}^+$ ion's clock transition, and η represents a minor dynamic correction that arises from the energy-level structure of the $^{40}\text{Ca}^+$ ion and the spectral distribution of the BBR field [39]. Compared to room-temperature optical clocks, the liquid-nitrogen cryogenic environment reduces the ambient temperature by approximately a factor of 4, leading to a reduction of the BBR shift uncertainty by more than 200 times with a similar evaluated temperature uncertainty. Consequently, the uncertainty in the BBR shift caused by $\Delta\alpha_0$ and η is on the order of 10^{-21} .

Compared to the first-generation liquid-nitrogen cryogenic $^{40}\text{Ca}^+$ ion optical clock, we have made several key improvements in the design and assembly of the BBR cavity, ion trap, and electrodes. As shown in Fig. S1, the ventilation holes in the BBR cavity—originally included to maintain vacuum consistency with the external chamber—are now sealed with oxygen-free copper covers to effectively block thermal radiation from the room-temperature environment. Additionally, to enhance temperature uniformity among the ion trap, ion trap holder, endcap electrodes, BBR cavity, and bottom of the Liquid-Nitrogen Cryogenic container (LNC), thin silver foils are inserted at the mechanical interfaces to enhance thermal contact and ensure their temperatures closely track that of the LNC. Furthermore, phosphor-bronze wires are employed as the conductors for both temperature sensors and electrodes. Before entering the BBR cavity, these wires are wound around the LNC several times to ensure their temperatures fully equilibrate with that of the LNC. Collectively, these modifications significantly enhance the temperature uniformity of the ambient environment.

We used PT100 thermistors in a three-wire configura-

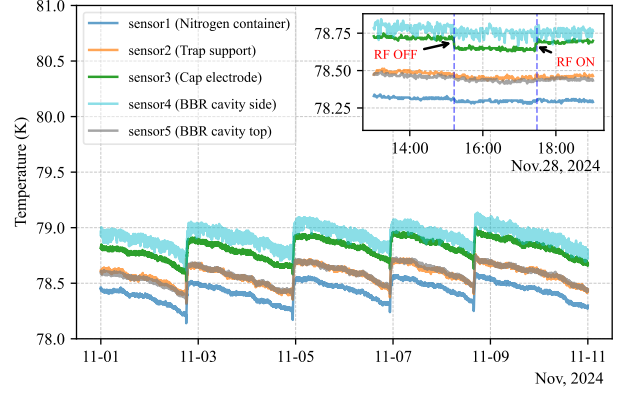


FIG. 1. Temperature measurements of the LNCIOC Ca^{+2} ion optical clock 2. The abrupt temperature drops are due to the periodic refilling of liquid nitrogen.

tion to eliminate temperature measurement errors from wire resistance. All sensors were individually calibrated to an accuracy of 0.1 K over the 75–85 K temperature range. In LNCIOC Ca^{+2} , five sensors were employed to monitor the temperatures at the bottom of the LNC, the endcap electrodes, the ion trap holder, and the BBR cavity. See Fig. S1(c) in the supplementary material for the detailed locations of these components.

To directly assess the temperature of the ion trap, we constructed a replica system with an identical ion-trapping setup and BBR cavity to that of LNCIOC Ca^{+2} . An additional temperature sensor was attached to the ion trap within this replica system. The ion trap exhibits the highest temperature among all components, due to its direct connection to four electrodes. When the RF is switched on or off, a temperature change of approximately 0.4 K is observed (see Fig. S2). We took the upper and lower bounds of all temperature sensors—spanning both the operational and replica systems—yielding a temperature estimate of 79.5 ± 1.4 K (see Fig. 1 and Fig. S2). Considering the 0.1 K calibration uncertainty, the final BBR temperature is evaluated as 79.5 ± 1.5 K, leading to a BBR uncertainty of 3.5×10^{-19} , nearly an order of magnitude lower compared to the first-generation liquid-nitrogen cryogenic $^{40}\text{Ca}^+$ optical clock.

Second-order Doppler shift—We implemented 3D sideband cooling in LNCIOC Ca^{+2} to suppress the second-order Doppler shift. Due to small Lamb-Dicke parameters for the 3D secular motions, which are $\eta_x = 0.025$, $\eta_y = 0.027$, and $\eta_z = 0.043$ respectively, the second-order sidebands are too weak to be experimentally resolved [40]. Therefore, we sequentially selected three first-order red sidebands to reduce the occupation numbers. Detailed sequences are illustrated in Fig. S2.

Results of 3D sideband cooling are shown in Fig. 2.

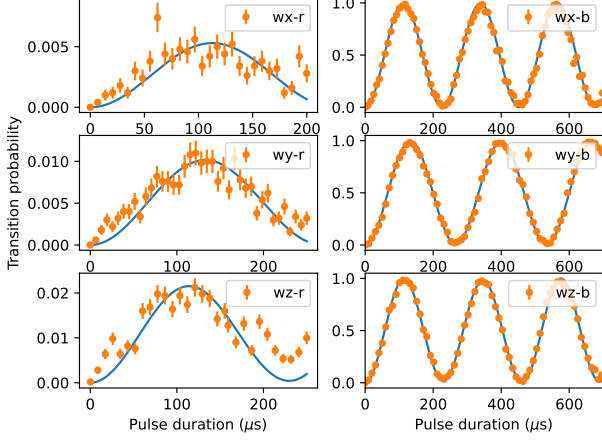


FIG. 2. Red- and blue-sideband Rabi oscillations for the three motional modes after sideband cooling. The orange dots represent the experimentally measured transition probabilities, and the blue solid lines are thermal-distribution fits to these data.

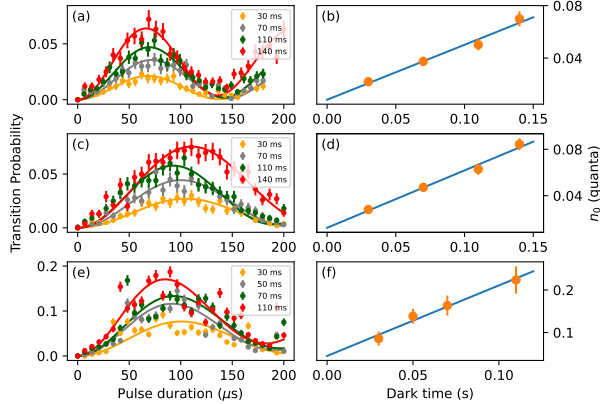


FIG. 3. Measurement of the heating rates. Panels (a), (c), and (e) present red-sideband Rabi oscillations of the X -, Y -, and Z -motional modes, respectively, measured at different dark times following sideband cooling. By fitting these curves with thermal-distribution models, the mean occupation numbers at different delays are extracted. (b), (d), and (f) show linear fits to the data in (a), (c), and (e), respectively. The slope of each fit corresponds to the heating rate, and the intercept gives the mean occupation number after sideband cooling. All fit results include 95% confidence intervals as uncertainty estimates.

Assuming that the Fock-state distribution is thermal after sideband cooling, we extract the mean occupation number, \bar{n} , by fitting the experimental data of the red-sideband Rabi oscillation. Furthermore, as shown in Fig. 3, by inserting a ‘dark time’ ranging from 30 to 140 ms between sideband cooling and red-sideband interrogation, we extracted the heating rates due to ambient

TABLE I. Evaluation of the second-order Doppler shift for LNCIOC Ca^{+2} .

	x	y	z
$\omega/2\pi$ (MHz)	3.531	3.166	2.580
η	0.025	0.027	0.043
TD/quantum (10^{-19})	3.9	3.5	2.9
n_0 (quanta)	0–0.03	0–0.04	0–0.11
\dot{n} (quanta/s)	0.43(7)	0.53(12)	1.31(43)
Total [10^{-19}]	-5.8 ± 0.4		

electric field noise. The heating effect can rapidly drive the Fock state towards a thermal distribution, however, the Fock-state distribution after sideband cooling may not initially be thermal [3, 41]. Therefore, to address the mean occupation number after sideband cooling, except using the thermal-distribution fitting, we also utilized the intercept derived from a linear fit to the heating rate measurements.

Over a period of nearly one month, we carried out five repeated measurements of both the initial mean occupation numbers after sideband cooling and the heating rates, as presented in Fig. S4. Under an 80-ms interrogation time, the uncertainty in the second-order Doppler shift is evaluated to be 4×10^{-20} , as shown in Table I.

Second-order Zeeman shift—The output frequency of the $^{40}\text{Ca}^{+}$ ion optical clock is determined by averaging over the three pairs of Zeeman transitions mentioned above. By comparing the output frequencies of room-temperature $^{40}\text{Ca}^{+}$ ion optical clocks, we precisely measured the average second-order Zeeman coefficient α_z of the three pairs of Zeeman transitions. One clock served as a frequency reference, with its DC magnetic field fixed at a constant value B_0 , and another served as the modulated clock with varying dc magnetic fields B . The frequency difference δ_z between the two clocks was measured as a function of B and B_0 , and can be described by the relation [21]:

$$\delta_z = \alpha_z(B^2 - B_0^2). \quad (2)$$

By varying the DC magnetic field B of the modulated clock, we obtained a set of frequency differences between the two clocks, as shown in Fig. S6. A linear fit to these data yielded $\alpha_z = 14.345(40) \text{ Hz/mT}^2$. The uncertainty of α_z was determined from the 95% confidence interval of the fit.

We derived the DC magnetic field of LNCIOC Ca^{+2} from the measured Zeeman splittings, determining it to be $37.197(1) \mu\text{T}$, corresponding to a second-order Zeeman shift of $-5.8 \pm 0.4 \times 10^{-19}$.

man shift uncertainty of 1.4×10^{-19} . Although the DC magnetic field may exhibit significant drift over a long period, daily variations remain well within this uncertainty budget.

Furthermore, due to imperfections in the trap symmetry, the RF field generates an oscillating magnetic field at the ion's position, with a frequency equal to that of the RF [42]. This RF-induced AC magnetic field can be characterized by measuring its effect on the ratio of Landé g -factors associated with the clock transition [43, 44]. The root mean square of the y -component of the AC magnetic field were measured to be $\langle B_y^2 \rangle = 11(9) \times 10^{-14} \text{ T}^2$. This yields an estimated upper bound of 4×10^{-21} for the second-order Zeeman shift.

Excess micromotion (EMM) shift—There exists a magic drive frequency of 24.801(2) MHz for the $^{40}\text{Ca}^+$ ion clock transition, at which the EMM-induced second-order Doppler shift and the Stark shift cancel out [34, 45]. The RF frequency was set to 24.801 MHz for LNCIOC Ca^{+2} to minimize the EMM shift. Through long-term measurements of the sideband spectra in three mutually perpendicular directions, the frequency shift caused by EMM is evaluated to be $(0 \pm 1.4) \times 10^{-19}$.

Background gas collisions—The collision-induced frequency shift (CFS) arising from interactions with background helium gas is evaluated using a nonperturbative quantum channel framework developed by A. C. Vutha [46]. This method has been validated in prior studies involving Sr^+ [46] and Al^+ [47, 48] ions colliding with He and H_2 . As it is not feasible to measure the pressure inside the BBR cavity, we use the pressure measured in the ambient room-temperature environment outside the BBR cavity, which is $3 \times 10^{-9} \text{ Pa}$, as an overestimation of the pressure within the BBR cavity. For the background gas at a temperature of 78.5 K, a particular calculation approach yields a collision frequency shift of 1.8×10^{-19} . Details can be found in the Supplementary Material.

Other shifts—The hyper Ramsey excitation scheme was employed to suppress the AC Stark shift induced by the clock laser [1, 16] and the chirp effect of the acousto-optic modulator (AOM) [49], ensuring that both frequency shifts are less than 1×10^{-19} . The total systematic frequency shifts of LNCIOC Ca^{+2} are presented in Table II.

Conclusion—We have developed a second-generation liquid-nitrogen cryogenic $^{40}\text{Ca}^+$ ion optical clock with an uncertainty of 4.6×10^{-19} , which represents an improvement of approximately one order of magnitude compared to our previous result [16]. It is the lowest reported uncertainty among all optical clocks to date. The cryogenic environment not only significantly reduces the BBR shift and its uncertainty, but also markedly reduces the heating rates caused by ambient electric field noise. As the performance of ion optical clocks continue to improve, the heating effect has gradually become one of the main limiting factors for the system uncertainty and ion coher-

TABLE II. Systematic shifts and uncertainties of the LNC $^{40}\text{Ca}^+$ ion optical clock 2.

Effect	Shift (10^{-19})	Uncertainty (10^{-19})
BBR	45.5	3.5
Excess micromotion	0.0	1.4
Secular motion	-5.8	0.4
Quadratic Zeeman (DC)	482.9	1.4
Quadratic Zeeman (AC)	0.0	0.04
Background gas	0.0	1.8
Residual 1st Zeeman	0.0	0.2
Electric quadrupole	0.0	0.1
AOM phase chirp	0.0	1.0
Clock laser Stark	0.0	0.6
Total	522.6	4.6

ence time of optical clocks. Our research experimentally confirms the remarkable suppression effect of the cryogenic environment on the heating rate, thereby offering a viable approach for enhancing the performance of ion optical clocks.

For LNCIOC Ca^{+2} , the BBR shift remains the primary contributor to the systematic uncertainty. Developing $^{40}\text{Ca}^+$ ion optical clocks cooled with helium at even lower temperatures or employing more accurate temperature assessment schemes holds promise for further reducing the BBR shift to the order of 10^{-20} . Meanwhile, by creating conditions to measure the ion exchange rate between two ions, one can precisely evaluate the vacuum level in directly cooled single-ion optical clocks. Additionally, developing a more comprehensive theoretical model for the collision frequency shift will enable further reduction of the background gas collision-induced frequency shift. In the next step, we will also enhance the performance of the clock laser and magnetic shielding to extend the clock interrogation time, aiming to achieve a $^{40}\text{Ca}^+$ ion optical clock with $10^{-16}/\sqrt{\tau}$ level stability. This, in turn, will allow the application of the 10^{-19} -level precision of the $^{40}\text{Ca}^+$ ion optical clock to precision measurements such as the frequency ratio between different optical clocks, the time variation of the fine-structure constant α , and the determination of millimeter-level height differences and tidal potentials.

Acknowledgements—We are deeply grateful to Bing Yan for providing the Ca^+ -He potential data, and to A. C. Vutha for helpful discussions. This work is supported by the National Key R&D Program of China

(Grant Nos. 2022YFB3904001 and 2022YFB3904004), Innovation Program for Quantum Science and Technology (Grant No. 2021ZD0300901), the National Natural Science Foundation of China (Grant Nos. 12204494, 12121004, 12320101003, 11934014, 12374235 and 12174402), the CAS Youth Innovation Promotion Association (Grant No Y2022099), the Natural Science Foundation of Hubei Province (Grant Nos. 2022CFA013 and 2023EHA006), the CAS Project for Young Scientists in Basic Research (Grant Nos. YSBR-055 and YSBR-085), and Strategic Priority Research Program of the Chinese Academy of Sciences (XDB0920101 and XDB0920202).

SUPPLEMENTAL MATERIAL

blackbody radiation (BBR)

As shown in Fig. 4(a), the liquid nitrogen container (LNC) is made of oxygen-free copper. The thermal conduction between the cryogenic LNC and the room-temperature vacuum chamber is effectively suppressed by the ultra-high vacuum environment. Four hollow cylindrical rods, made of stainless steel with low thermal conductivity, are mounted on the top of the LNC. These rods serve dual purposes: mechanically securing the LNC to the vacuum chamber and functioning as channels for both venting evaporated nitrogen and refilling liquid nitrogen. The LNC has a total volume of approximately 13 L, with a liquid nitrogen consumption rate of 3.5 L/day, and the frequency of replenishing liquid nitrogen into the LNC is approximately every 2 days.

The ion trap system—including the trap itself, cap electrodes, trap support, and the BBR cavity—is thermally anchored to the LNC to maintain cryogenic conditions. The ion trap and cap electrodes are mounted atop the trap support. Electrical insulation between the cap electrodes and the support is provided by alumina ceramic sheets, with thin silver foils applied on both sides to maintain thermal continuity (Fig. 4(c)). The lower part of the ion trap, made of diamond, is mounted directly onto the support without insulation, but silver foils are inserted at the contact surfaces to enhance thermal conduction. The trap support and BBR cavity are secured to the LNC through M6 threaded holes, with silver foils at the interfaces to maximize heat transfer. The RF electrodes are connected to external electronics via a thermally isolating path consisting of stainless-steel rods and phosphor-bronze wires routed through the BBR cavity, ensuring efficient RF delivery while minimizing heat leakage.

Temperature monitoring is achieved using a cylindrical temperature sensor, which is wrapped in silver foil and inserted into a custom-designed copper mounting structure with a precision-matched hole to increase the contact area between the temperature sensor and the component to be measured. After the temperature sensor is wrapped with thin silver foil, it is fixed in the small hole of the mounting structure with an M1.6 screw. The mounting structure is installed at the position to be measured through M4 threaded holes. This design ensures reliable thermal coupling for accurate temperature readout.

Second-order Doppler shift

The Zeeman transition $|S_{1/2}, m = 1/2\rangle \rightarrow |D_{5/2}, m = -1/2\rangle$ was selected as the carrier. As shown in Fig. 4(b), two beams of σ^+ and σ^- circularly

polarized 397 nm lasers are employed for state preparation. Additionally, a 729 nm clock laser beam (beam 2 in Fig. 4(b)) with a power of approximately 15 mW is used for sideband cooling. After beam expansion, beam 2 is tightly focused onto the ion position to minimize its waist, resulting in a π -pulse length of approximately $2 \mu\text{s}$ for the carrier transition, corresponding to a π -pulse time of several tens of microseconds for the first-order secular motion sidebands. Three first-order red-sideband pulses, corresponding to the three motional modes (denoted as x , y , and z), are sequentially applied to the Ca^+ ion. Based on the selection rules for the electric quadrupole transition, beam 2 can excite only two pairs of Zeeman transitions with $\Delta m = \pm 1$. After state preparation, the number of observable Zeeman transitions is halved, with minimal impact of off-resonant carrier transitions. A radial secular motion frequency stabilization device ensures that the frequency of the clock laser remains resonant with the red sidebands over a protracted period.

Sideband cooling for any motional mode can inadvertently heat the others [3]. Therefore, the three modes were cooled in an alternating and sequential manner. Each cooling cycle for a given motional mode consists of a $5 \mu\text{s}$ state-preparation pulse, a $10\text{--}30 \mu\text{s}$ red-sideband pulse, and a $5 \mu\text{s}$ 854-nm pulse to depopulate the $D_{5/2}$ state. As the sideband cooling proceeds, the mean occupation number decreases, and correspondingly, the average Rabi frequency of the red sideband also decreases [40]. To sustain a high probability of sideband transition, the durations of the red-sideband pulses are linearly increased in accordance with the number of cooling cycles. In addition, a dark time is inserted between the sideband-cooling and clock-interrogation sequences to characterize the heating rates of the three motional modes due to ambient electric field noise. The clock interrogation can be used to measure the Rabi oscillation of the red sideband or to operate the clock using the hyper-Ramsey excitation. The full timing sequence is depicted in Fig. 6.

To evaluate the Doppler cooling performance, we experimentally measured the Rabi oscillations of the carrier for both clock laser beam 1 and beam 3 after Doppler cooling and after sideband cooling, respectively (see Fig. 8). According to the Debye-Waller effect [40], the Rabi frequencies satisfy the following relationships:

$$e^{-(\eta_x^1)^2 \bar{n}_x + (\eta_y^1)^2 \bar{n}_y + (\eta_z^1)^2 \bar{n}_z} = \frac{\Omega_{\text{Doppler},1}}{\Omega_{\text{SC},1}}, \quad (3)$$

$$e^{-(\eta_x^3)^2 \bar{n}_x + (\eta_y^3)^2 \bar{n}_y} = \frac{\Omega_{\text{Doppler},3}}{\Omega_{\text{SC},3}}, \quad (4)$$

where η_i^1 ($i = x, y, z$) and η_i^3 ($i = x, y$) are the Lamb-Dicke parameters of beam 1 and beam 3, respectively,

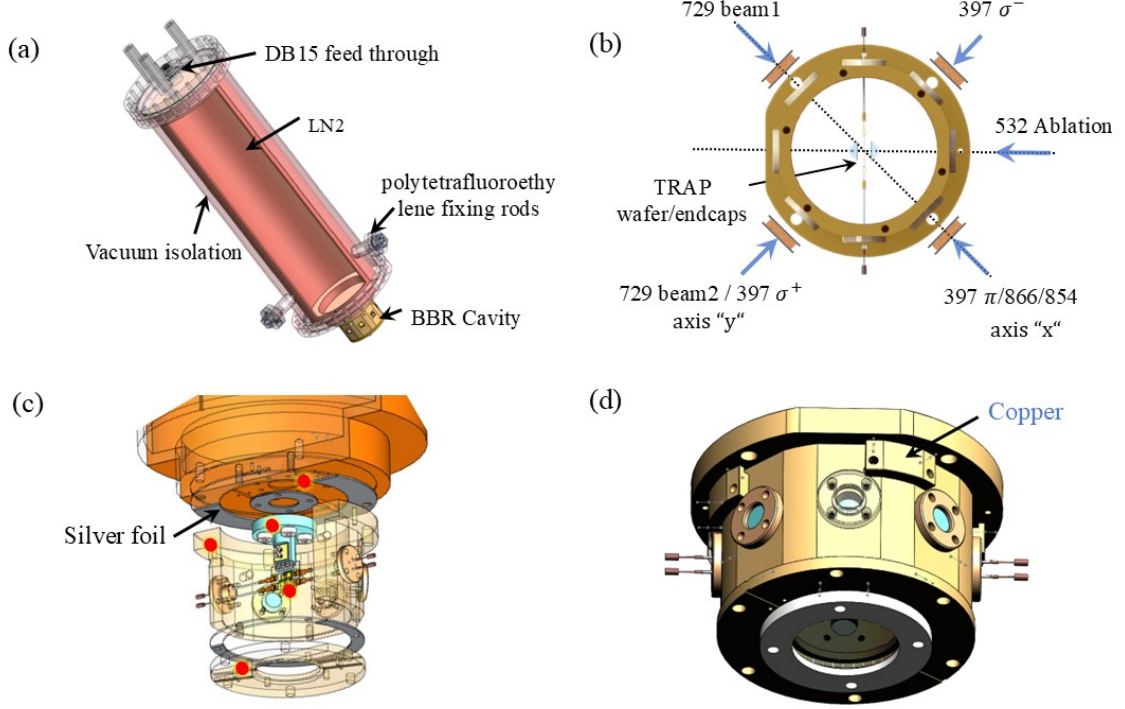


FIG. 4. (a) An inverted schematic diagram of the ion trap apparatus. The ion trap is surrounded by the BBR cavity externally, and both are mounted at the bottom of a liquid nitrogen container (LNC), thereby exposing the $^{40}\text{Ca}^+$ ion to the cryogenic environment of liquid nitrogen. The red dots indicate the installation positions of the temperature sensors. (b) Optical layout diagram. All the lasers shown in the figure lie in the same horizontal plane. There is an additional clock laser beam (beam 3) in the vertical direction (not depicted here) that is used to detect the micromotion sideband. The 532 nm laser is employed for ion generation through laser ablation, while the other lasers are used for cooling, repumping, state preparation, clock interrogation, and state detection. (c) LNC container and vacuum setup. The yellow metallic-colored part is an Oxygen-Free High Conductivity copper LNC, featuring four vents on the top for the injection and evaporation of liquid nitrogen. The LNC is housed within a vacuum outer chamber, which includes three polytetrafluoroethylene (PTFE) thimbles that stabilize the LNC and suppress horizontal displacement. Due to the excellent thermal conductivity of oxygen-free copper, variations in the liquid nitrogen level cause negligible thermal expansion or contraction of the container. The ion trap confinement device and the BBR cavity are installed in an inverted configuration beneath the LNC. (d) Schematic diagram of the BBR cavity. There are three small ventilation holes on the BBR cavity, and each hole is equipped with a copper cover plate to block the thermal radiation from the room-temperature environment. A reasonable spacing (5 mm) is set between the cover plate and the ventilation hole. This not only balances the air pressure but also almost eliminates the thermal radiation from the external room-temperature environment experienced by the $^{40}\text{Ca}^+$ ion.

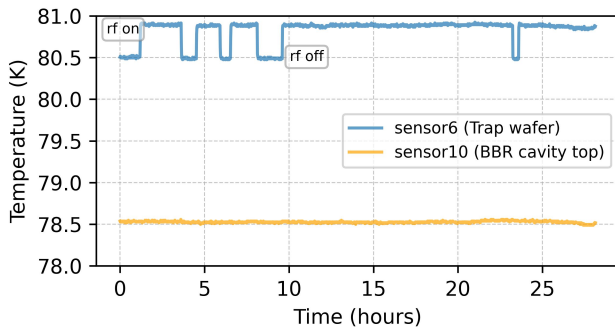


FIG. 5. Sensor 6 is directly mounted on the surface of the ion trap and secured by a mechanical fixture.

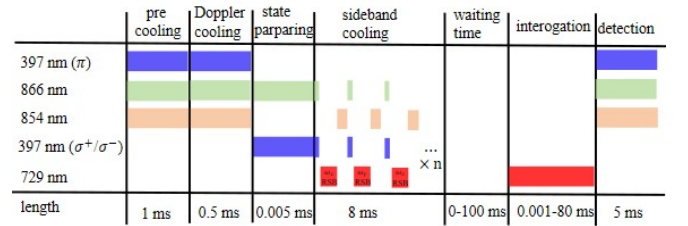


FIG. 6. Pulses sequence. During the sideband-cooling phase, the three motional modes are cooled sequentially, with 100 cooling cycles for each mode. The pulse duration of the red-sideband for motional modes X and Y increases linearly from $10\mu\text{s}$ to $30\mu\text{s}$, while for motional mode Z , it increases from $12\mu\text{s}$ to $22\mu\text{s}$.

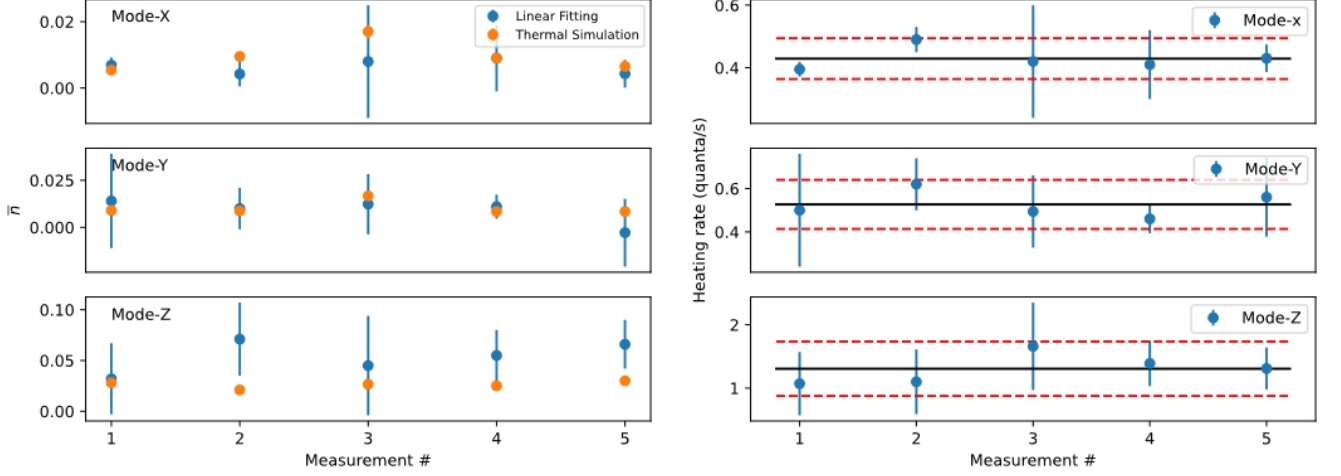


FIG. 7. Measurement results of the heating rates and the mean occupation numbers after sideband cooling for motional modes X, Y and Z. (a) The orange dots and the blue dots represent the mean occupation numbers after sideband cooling, which were obtained through the thermal distribution fitting and the heating rate measurement, respectively. (b) The blue dots represent the measured heating rates, the black solid line indicates the average value of the heating rates, and the range enclosed by the red dashed lines represents the 2σ interval of the measured heating rates.

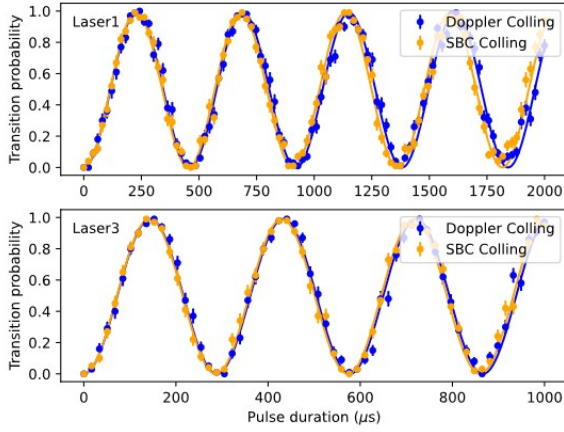


FIG. 8. Rabi oscillations of clock laser beams 1 and 3. The blue and yellow dots represent the experimental data after Doppler cooling and sideband cooling, respectively. The blue and yellow solid lines are the sine fits to the corresponding experimental data, yielding $\Omega_{\text{Doppler},1} = 2.172(4)$ MHz, $\Omega_{\text{SC},1} = 2.201(4)$ MHz, $\Omega_{\text{Doppler},3} = 3.464(5)$ MHz, and $\Omega_{\text{SC},3} = 3.488(8)$ MHz.

for the corresponding secular motion modes. $\Omega_{\text{Doppler},j}$ and $\Omega_{\text{SC},j}$ ($j = 1, 3$) represent the Rabi frequencies after sideband cooling, respectively. The experimental results are shown in Fig. 7. Due to the geometric characteristics of the optical path, $\eta_x \approx \eta_y$, assuming $\bar{n}_x = \bar{n}_y$, we obtained $\bar{n}_x = \bar{n}_y = 2.6$ and $\bar{n}_z = 4.8$. Then, the average temperature was asserted to be $T_{\text{avg}} = 0.76$ mK, which is close to the Doppler cooling limit of 0.52 mK for the

$^{40}\text{Ca}^+$ ion.

Quadratic Zeeman coefficient

Both optical clocks operate at room temperature, and the systematic frequency shift difference between them is assessed to be $(10.7 \pm 39.0) \times 10^{-18}$, which is mainly limited by the BBR shift. The schematic of the comparison link and the corresponding experimental results are shown in Fig. 9 and Fig. 10, respectively.

EMM shift

EMM can cause the second-order Doppler shift and the Stark shift, which can be expressed as [50]:

$$\frac{\Delta\nu_{\text{MM}}}{\nu_0} = - \left(\frac{\Omega}{2\pi\nu_0} \right)^2 \left[1 + \frac{\Delta\alpha_0}{h\nu_0} \left(\frac{m\Omega c}{e} \right)^2 \right] \sum_{i=1}^3 R_i^2, \quad (5)$$

where ν_0 is the clock transition frequency, Ω is the RF frequency, $\Delta\alpha_0$ is the difference in the static polarizabilities between the ground and excited energy levels of the clock transition, m is the ion mass, e is the elementary charge, h is the Planck constant, and R_i is the intensity ratio of the micromotion sideband to that of the carrier, measured by the i -th clock laser beam. Experimentally, we employed three mutually orthogonal clock laser beams to probe the micromotion sidebands along independent spatial directions. EMM suppression was performed once by optimizing the sideband amplitudes after each refilling of

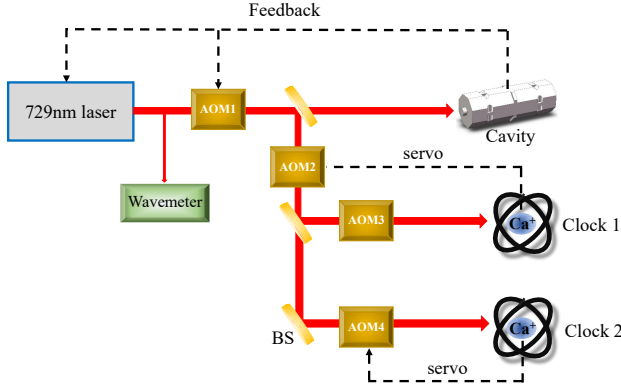


FIG. 9. Schematic diagram of the frequency comparison link. The optical paths between the 729-nm laser and the ultra-stable cavity, as well as between the 729-nm laser and the physical systems of the $^{40}\text{Ca}^+$ ion optical clocks, are connected via optical fibers, and we have implemented fiber noise suppression on all fiber links. The feedback signal from the ultra-stable cavity acts on AOM1 to reference the frequency of the clock laser to the ultra-stable cavity. For clock 1, after being jointly modulated by AOM2 and AOM1, the frequency of laser 1 is referenced to clock 1. The power of the RF applied to AOM2 is fixed, but its frequency is sequentially varied during the probing process to resonate different Zeeman transitions. The frequency of the RF applied to AOM3 is fixed, but its amplitude is modulated to change the power of laser 1. For clock 2, both the frequency and power of the RF applied to AOM4 are modulated. Since both laser 1 and laser 2 pass through the same AOM2, the frequency difference applied to AOM4 and AOM3 represents the frequency difference between clock 2 and clock 1.

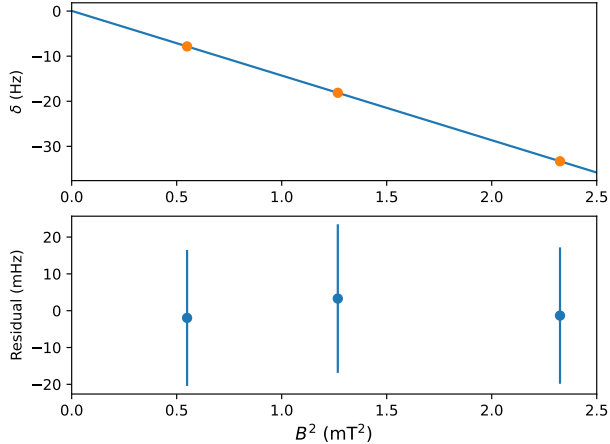


FIG. 10. Measurement of the quadratic Zeeman coefficient α_z . The orange dots represent the measured frequency differences between the two optical clocks. The blue solid line is a linear fit of the experimental data. The lower panel shows the residuals of the experimental data relative to the fit.

liquid nitrogen. Over a two-months period, we randomly sampled the Rabi frequency ratios between the micro-motion sidebands and the carriers along all three axes. As shown in Figure 11, the frequency shift induced by EMM was evaluated to be $(0 \pm 1.4) \times 10^{-19}$, which is mainly caused by the magnitude of R_i and the uncertainty in $\Delta\alpha_0$. It is worth noting that in the cryogenic optical clock, the RF-induced AC magnetic field is relatively small; Consequently, the micromotion sidebands it causes are negligible.

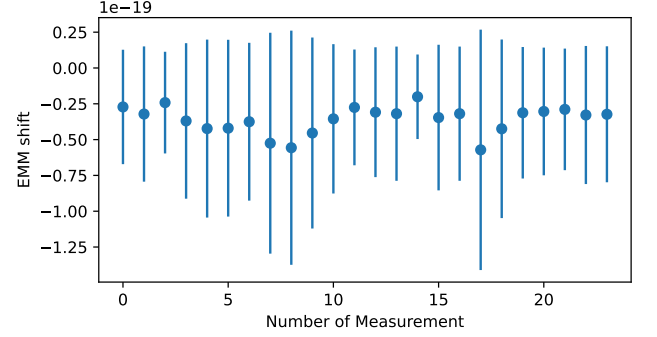


FIG. 11. Measured second-order Doppler and Stark shifts caused by excess micromotion (EMM) in multiple runs.

Quadratic Zeeman (AC) shift

As indicated in Ref. [42], the quadratic Zeeman shift caused by the component B_{\parallel} of the AC magnetic field B_{AC} that is parallel to the quantization axis has the same generation mechanism as the quadratic Zeeman shift induced by the DC magnetic field B_0 . In contrast, the quadratic Zeeman shift arising from the component B_{\perp} of B_{AC} that is perpendicular to the quantization axis is proportional to the magnetic quantum number m . It does not shift the center of a pair of Zeeman transitions but causes a deviation in the measured Zeeman splitting, thereby affecting the measurement of the ratio of the Landé g -factor. The specific expression is as follows [44]:

$$r = \frac{\left[1 + \frac{1}{2} \frac{\omega_D^2}{\omega_S^2 - \Omega_{RF}^2} \frac{\langle B_{\perp}^2 \rangle}{B_0^2} \right]}{\left[1 + \frac{1}{2} \frac{\omega_S^2}{\omega_D^2 - \Omega_{RF}^2} \frac{\langle B_{\perp}^2 \rangle}{B_0^2} \right]} \frac{g_D}{g_S} \quad (6)$$

where r is the ratio of the Landé g -factor between the excited and ground energy levels of the $^{40}\text{Ca}^+$ ion clock transition, which is measured through the relationship between two pairs of Zeeman transitions. The ratio g_D/g_S represents the unperturbed value. ω_D and ω_S are the Zeeman splittings of the $D_{5/2}$ state and $S_{1/2}$ state, respectively, under a DC magnetic field B_0 .

In order to measure the y -direction component of the AC magnetic field, we modulated the DC mag-

netic field in the x -direction with a magnitude of $56.363(5) \mu\text{T}$. By locking onto two pairs of Zeeman transitions, namely $|S_{1/2}, m = \mp 1/2\rangle \rightarrow |D_{5/2}, m = \mp 3/2\rangle$ and $|S_{1/2}, m = \pm 1/2\rangle \rightarrow |D_{5/2}, m = \mp 1/2\rangle$, we measured $r = 0.599488818(9)$. Then, using the precisely measured value of the ratio g_D/g_S and equation (6), we calculated $\langle B_\perp^2 \rangle = \langle B_y^2 \rangle + \langle B_z^2 \rangle = 11(9) \times 10^{-14} \text{ T}^2$. Its uncertainty is mainly limited by the precision of g_D/g_S .

Since the DC magnetic field is in the y -direction during the operation of the optical clock, only the y -component B_y of the AC magnetic field will cause a quadratic Zeeman shift to the center of a pair of Zeeman transitions. The upper range of $\langle B_y^2 \rangle$ is $1(1) \times 10^{-13} \text{ T}^2$, and the corresponding quadratic Zeeman shift caused by the AC magnetic field induced by the RF drive is 4×10^{-21} .

Although higher precision in evaluating the RF-induced AC magnetic field can be achieved by measuring the Autler-Townes splitting and Zeeman precession [42, 43]. However, due to constraints from the magnetic shielding structure, it is difficult for the current coil of the LNCIOC $^{40}\text{Ca}^+$ system to generate a DC magnetic field that satisfies the resonance condition between the two sublevels of the $S_{1/2}$ state and the RF frequency.

Background gas collisions

The collisional frequency shift (CFS), arising from collisions with background helium gas, is calculated using a nonperturbative analytic framework based on a quantum channel description of the scattering process developed by A. C. Vutha et al. This method has been validated through calculations of the fractional frequency shifts for Sr^+ and Al^+ ions colliding with helium and H_2 . The expression for the CFS correction is [51]:

$$\begin{aligned} \delta\omega &= n_{bg} v \frac{4\pi}{k^2} \sum_l (2l+1)(A_l + B_l), \\ A_l &= \frac{1}{4}(\sin 2\phi_{l,e} - \sin 2\phi_{l,g}), \\ B_l &= |\sin \phi_{l,e} \sin \phi_{l,g}| \sin(\phi_{l,e} - \phi_{l,g}). \end{aligned} \quad (7)$$

here, $\phi_{l,g}$ and $\phi_{l,e}$ denote the l -th partial wave scattering phase shifts for the ground and excited clock states, respectively. We calculated the phase shifts based on potential energy curves for the Ca^+ -He system that adiabatically connect to the ground ($S_{1/2}$) and excited ($D_{5/2}$) electronic states. These curves were taken from Ref. [52], where they were computed using the MOLPRO 2010 quantum chemistry package. The calculations employed the multireference configuration interaction (MRCI) method to accurately capture the interaction potentials.

The scattering wave functions were obtained by numerically integrating the Schrödinger equation for each partial wave, with angular momentum values ranging from

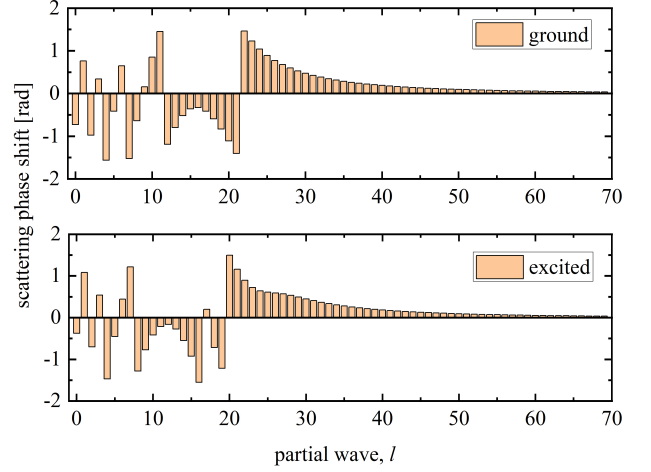


FIG. 12. An example of calculated scattering phase shifts at a collision energy 100 K. The phase shift are shown as a function of the partial wave angular momentum, l , for collisions of He with Ca^+ in the ground S and excited D states.

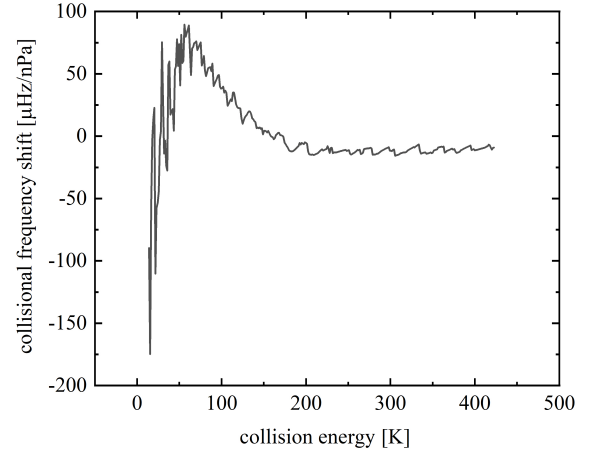


FIG. 13. Collision frequency shifts for the Ca^+ clock transition as a function of collision energy due to helium collisions.

$l = 0$ to 70. The partial wave phase shifts for Ca^+ -He scattering at a collision energy of 100 K are shown in Fig. 12. These phase shifts were computed using the Ca^+ -He potential energy curves that adiabatically connect to the ground ($S_{1/2}$) and excited ($D_{5/2}$) clock states. For the excited state, the potential energy curves corresponding to $\Lambda = 0, 1, 2$ were averaged with equal weights to construct an effective $D_{5/2}$ potential. The resulting CFS, as a function of collision energy, is also presented in the Fig. 13. To obtain the thermally averaged CFS, a Boltzmann-weighted average over collision energies was performed at a temperature of 78.5 K. The final thermally averaged CFS was found to be $42 \mu\text{Hz}$ at a back-

ground gas pressure of $P = 3$ nPa. To evaluate the sensitivity of our result to uncertainties in the interaction potential, we varied the potential depth by 1% and observed a 10% change in $\langle\delta\omega\rangle$ at the same pressure. In an ultra-high-vacuum trapped-ion clock, the dominant residual gases are helium and hydrogen molecules. Because no accurate Ca^+-H_2 potential is available, we estimated the CFS due to H_2 by scaling the known Ca^+-He shift using the long-range C_4/r^4 scattering model. In the worst-case limit, the shift scales as $\delta\omega \sim n_{\text{bg}} v \sigma$, where σ is the elastic cross section for ion-atom collision derived in Ref. [53]:

$$\sigma = \pi \left(1 + \frac{\pi^2}{16}\right) \left(\frac{\mu C_4}{\hbar^2 E}\right)^{1/3} \propto (\mu \alpha)^{1/3}. \quad (8)$$

Here μ is the reduced mass and α the static polarizability. Using $\alpha_{\text{He}} = 1.38 a_0$ [54] and $\alpha_{\text{H}_2} = 5.4 a_0$ [55], we find $\frac{\delta\omega_{\text{H}_2}}{\delta\omega_{\text{He}}} \approx 1.8$. Thus, at $P = 3$ nPa the CFS due to hydrogen is estimated to be $\langle\delta\omega\rangle = 74 \mu\text{Hz}$. For the $\omega_0 = 411$ THz Ca^+ clock transition, this corresponds to a fractional shift $\frac{\langle\delta\omega\rangle}{\omega_0} \approx 1.8 \times 10^{-19}$. We estimate the upper bound of the collisional frequency shift to be approximately 1.8×10^{-19} .

* These authors contributed equally to this work.

† yaohuang@apm.ac.cn

‡ guanhua@apm.ac.cn

§ klgao@apm.ac.cn

- [1] N. Huntemann, B. Lipphardt, M. Okhapkin, C. Tamm, E. Peik, A. V. Taichenachev, and V. I. Yudin, *Phys. Rev. Lett.* **109**, 213002 (2012).
- [2] P. Dubé, A. A. Madej, M. Tibbo, and J. E. Bernard, *Phys. Rev. Lett.* **112**, 173002 (2014).
- [3] J.-S. Chen, S. M. Brewer, C. W. Chou, D. J. Wineland, D. R. Leibbrandt, and D. B. Hume, *Phys. Rev. Lett.* **118**, 053002 (2017).
- [4] S. Häfner, S. Falke, C. Grebing, S. Vogt, T. Legero, M. Merimaa, C. Lisdat, and U. Sterr, *Opt. Lett.* **40**, 2112 (2015).
- [5] E. Oelker, R. B. Hutson, C. J. Kennedy, L. Sonderhouse, T. Bothwell, A. Goban, D. Kedar, C. Sanner, J. M. Robinson, G. E. Marti, D. G. Matei, T. Legero, M. Giunta, R. Holzwarth, F. Riehle, U. Sterr, and J. Ye, *Nature Photonics* **13**, 714 (2019).
- [6] K. J. Arnold, R. Kaewuam, S. R. Chanu, T. R. Tan, Z. Zhang, and M. D. Barrett, *Phys. Rev. Lett.* **124**, 193001 (2020).
- [7] M. Steinell, H. Shao, M. Filzinger, B. Lipphardt, M. Brinkmann, A. Didier, T. E. Mehlstäubler, T. Lindvall, E. Peik, and N. Huntemann, *Phys. Rev. Lett.* **131**, 083002 (2023).
- [8] R. Lange, N. Huntemann, C. Sanner, H. Shao, B. Lipphardt, C. Tamm, and E. Peik, *Phys. Rev. Lett.* **125**, 143201 (2020).
- [9] C. W. Chou, D. B. Hume, J. C. J. Koelemeij, D. J. Wineland, and T. Rosenband, *Phys. Rev. Lett.* **104**, 070802 (2010).
- [10] K. J. Arnold, R. Kaewuam, A. Roy, T. R. Tan, and M. D. Barrett, *Nature Communications* **9**, 1650 (2018).
- [11] P.-L. Liu, Y. Huang, W. Bian, H. Shao, H. Guan, Y.-B. Tang, C.-B. Li, J. Mitroy, and K.-L. Gao, *Phys. Rev. Lett.* **114**, 223001 (2015).
- [12] A. Aeppli, K. Kim, W. Warfield, M. S. Safronova, and J. Ye, *Phys. Rev. Lett.* **133**, 023401 (2024).
- [13] M. Marshall, D. R. Castillo, W. Dworschack, A. Aeppli, K. Kim, D. Lee, W. Warfield, N. Nardelli, T. Fortier, J. Ye, *et al.* <https://doi.org/10.1103/hb3c-dk28> (2025).
- [14] S. M. Brewer, J.-S. Chen, A. M. Hankin, E. R. Clements, C. W. Chou, D. J. Wineland, D. B. Hume, and D. R. Leibbrandt, *Phys. Rev. Lett.* **123**, 033201 (2019).
- [15] I. Ushijima, M. Takamoto, M. Das, T. Ohkubo, and H. Katori, *Nature Photonics* **9**, 185 (2015).
- [16] Y. Huang, B. Zhang, M. Zeng, Y. Hao, Z. Ma, H. Zhang, H. Guan, Z. Chen, M. Wang, and K. Gao, *Phys. Rev. Appl.* **17**, 034041 (2022).
- [17] A. Tofful, C. F. A. Baynham, E. A. Curtis, A. O. Parsons, B. I. Robertson, M. Schioppo, J. Tunesi, H. S. Margolis, R. J. Hendricks, J. Whale, R. C. Thompson, and R. M. Godun, *Metrologia* **61**, 045001 (2024).
- [18] S. Dörscher, N. Huntemann, R. Schwarz, R. Lange, E. Benkler, B. Lipphardt, U. Sterr, E. Peik, and C. Lisdat, *Metrologia* **58**, 015005 (2021).
- [19] Z. Zhiqiang, K. J. Arnold, R. Kaewuam, and M. D. Barrett, *Science Advances* **9**, eadg1971 (2023).
- [20] J. Li, X.-Y. Cui, Z.-P. Jia, D.-Q. Kong, H.-W. Yu, X.-Q. Zhu, X.-Y. Liu, D.-Z. Wang, X. Zhang, X.-Y. Huang, M.-Y. Zhu, Y.-M. Yang, Y. Hu, X.-P. Liu, X.-M. Zhai, P. Liu, X. Jiang, P. Xu, H.-N. Dai, Y.-A. Chen, and J.-W. Pan, *Metrologia* **61**, 015006 (2024).
- [21] R. M. Godun, P. B. R. Nisbet-Jones, J. M. Jones, S. A. King, L. A. M. Johnson, H. S. Margolis, K. Szymaniec, S. N. Lea, K. Bongs, and P. Gill, *Phys. Rev. Lett.* **113**, 210801 (2014).
- [22] R. Lange, N. Huntemann, J. M. Rahm, C. Sanner, H. Shao, B. Lipphardt, C. Tamm, S. Weyers, and E. Peik, *Phys. Rev. Lett.* **126**, 011102 (2021).
- [23] C. Sanner, N. Huntemann, R. Lange, C. Tamm, E. Peik, M. S. Safronova, and S. G. Porsev, *Nature* **567**, 204 (2019).
- [24] S. Kolkowitz, I. Pikovski, N. Langellier, M. D. Lukin, R. L. Walsworth, and J. Ye, *Phys. Rev. D* **94**, 124043 (2016).
- [25] M. Filzinger, S. Dörscher, R. Lange, J. Klose, M. Steinell, E. Benkler, E. Peik, C. Lisdat, and N. Huntemann, *Phys. Rev. Lett.* **130**, 253001 (2023).
- [26] N. Dimarcq, M. Gertsvolf, and e. a. G Mileti, *Metrologia* **61**, 012001 (2024).
- [27] M. Takamoto, I. Ushijima, N. Ohmae, T. Yahagi, K. Kokado, H. Shinkai, and H. Katori, *Nature Photonics* **14**, 411 (2020).
- [28] W. F. McGrew, X. Zhang, R. J. Fasano, S. A. Schäffer, K. Bely, D. Nicolodi, R. C. Brown, N. Hinkley, G. Milani, M. Schioppo, T. H. Yoon, and A. D. Ludlow, *Nature* **564**, 87 (2018).
- [29] T. E. Mehlstäubler, G. Grosche, C. Lisdat, P. O. Schmidt, and H. Denker, *Reports on Progress in Physics* **81**, 064401 (2018).
- [30] H. Guan, B. Zhang, H. Zhang, Y. Huang, Y. Hao, M. Zeng, and K. Gao, *AVS Quantum Science* **3**, 044701 (2021).

- (2021).
- [31] B. Zhang, Y. Huang, H. Zhang, Y. Hao, M. Zeng, H. Guan, and K. Gao, *Chinese Physics B* **29**, 074209 (2020).
 - [32] Y. Huang, H. Guan, M. Zeng, L. Tang, and K. Gao, *Phys. Rev. A* **99**, 011401 (2019).
 - [33] M. Zeng, Y. Huang, B. Zhang, Y. Hao, Z. Ma, R. Hu, H. Zhang, Z. Chen, M. Wang, H. Guan, and K. Gao, *Phys. Rev. Appl.* **19**, 064004 (2023).
 - [34] P. Dubé, A. A. Madej, Z. Zhou, and J. E. Bernard, *Phys. Rev. A* **87**, 023806 (2013).
 - [35] Z. Ma, B. Zhang, Y. Huang, K. Gao, and H. Guan, *Acta Physica Sinica* **74**, 094204 (2025).
 - [36] M. Zeng, Y. Huang, B. Zhang, Z. Ma, Y. Hao, R. Hu, H. Zhang, H. Guan, and K. Gao, *Chinese Physics B* **32**, 113701 (2023).
 - [37] V. I. Yudin, A. V. Taichenachev, C. W. Oates, Z. W. Barber, N. D. Lemke, A. D. Ludlow, U. Sterr, C. Lisdat, and F. Riehle, *Phys. Rev. A* **82**, 011804 (2010).
 - [38] J. W. Farley and W. H. Wing, *Phys. Rev. A* **23**, 2397 (1981).
 - [39] S. G. Porsev and A. Derevianko, *Phys. Rev. A* **74**, 020502 (2006).
 - [40] D. J. Wineland, C. Monroe, W. M. Itano, D. Leibfried, B. E. King, and D. M. Meekhof, *Journal of research of the National Institute of Standards and Technology* **103**, 259 (1998).
 - [41] A. J. Rasmusson, M. D’Onofrio, Y. Xie, J. Cui, and P. Richerme, *Phys. Rev. A* **104**, 043108 (2021).
 - [42] H. C. J. Gan, G. Maslennikov, K.-W. Tseng, T. R. Tan, R. Kaewuam, K. J. Arnold, D. Matsukevich, and M. D. Barrett, *Phys. Rev. A* **98**, 032514 (2018).
 - [43] Z. Ma, B. Zhang, Y. Huang, R. Hu, M. Zeng, K. Gao, and H. Guan, *Phys. Rev. A* **110**, 063102 (2024).
 - [44] K. J. Arnold, R. Kaewuam, S. R. Chanu, T. R. Tan, Z. Zhang, and M. D. Barrett, *Phys. Rev. Lett.* **124**, 193001 (2020).
 - [45] D. J. Berkeland, J. D. Miller, J. C. Bergquist, W. M. Itano, and D. J. Wineland, *Journal of Applied Physics* **83**, 5025 (1998).
 - [46] A. C. Vutha, T. Kirchner, and P. Dubé, *Phys. Rev. A* **96**, 022704 (2017).
 - [47] A. M. Hankin, E. R. Clements, Y. Huang, S. M. Brewer, J.-S. Chen, C. W. Chou, D. B. Hume, and D. R. Leibbrandt, *Phys. Rev. A* **100**, 033419 (2019).
 - [48] J. Davis, P. Dubé, and A. C. Vutha, *Phys. Rev. Res.* **1**, 033137 (2019).
 - [49] S. Falke, M. Misera, U. Sterr, and C. Lisdat, *Applied Physics B* **107**, 301 (2012).
 - [50] P. Dubé, A. A. Madej, Z. Zhou, and J. E. Bernard, *Phys. Rev. A* **87**, 023806 (2013).
 - [51] J. Davis, P. Dubé, and A. C. Vutha, *Phys. Rev. Res.* **1**, 033137 (2019).
 - [52] H. Guo, *The collision of Ca ion with the rare-gas atoms: Interaction potential, spectrum and dynamics*, Master’s thesis, Jilin University (2020).
 - [53] R. Côté and A. Dalgarno, *Phys. Rev. A* **62**, 012709 (2000).
 - [54] J. Mitroy, M. S. Safronova, and C. W. Clark, *Journal of Physics B: Atomic, Molecular and Optical Physics* **43**, 202001 (2010).
 - [55] W. Kolos and L. Wolniewicz, *The Journal of Chemical Physics* **46**, 1426 (1967).